LAWRENCE
LIVERMORE
NATIONAL
LABORATORY

LLNL-TR-747137

MODAL FREQUENCY TRACKING: Performance Analysis on Noisy Experimental Ground Test Data

J. V. Candy, L. M. Stoops, S. N. Franco, M. C. Emmons

March 2, 2018

Disclaimer

This document was prepared as an account of work sponsored by an agency of the United States government. Neither the United States government nor Lawrence Livermore National Security, LLC, nor any of their employees makes any warranty, expressed or implied, or assumes any legal liability or responsibility for the accuracy, completeness, or usefulness of any information, apparatus, product, or process disclosed, or represents that its use would not infringe privately owned rights. Reference herein to any specific commercial product, process, or service by trade name, trademark, manufacturer, or otherwise does not necessarily constitute or imply its endorsement, recommendation, or favoring by the United States government or Lawrence Livermore National Security, LLC. The views and opinions of authors expressed herein do not necessarily state or reflect those of the United States government or Lawrence Livermore National Security, LLC, and shall not be used for advertising or product endorsement purposes.

This work performed under the auspices of the U.S. Department of Energy by Lawrence Livermore National Laboratory under Contract DE-AC52-07NA27344.

MODAL FREQUENCY TRACKING:

Performance Analysis

on

Noisy Experimental Ground Test Data

J. V. Candy, L. M. Stoops, S. N. Franco, M. C. Emmons

Executive Summary

Mechanical devices operating in an environment contaminated by noise, uncertainties, and extraneous disturbances lead to low signal-to-noise-ratios creating an extremely challenging signal processing problem—especially for on-line, real-time, in-flight application. In this report, we discuss a model-based approach to incorporate physical device features into a dynamic structure that can be used to perform on-line tracking of modal frequencies. The approach we take, after pre-processing the raw measurement data, is to obtain a representation of the structural device under test that captures its underlying response to a suite of excitations and operating conditions. One approach is to apply modern system identification techniques based on stochastic subspace methods capable of both: (1) identifying the underlying black-box structure enabling the extraction of structural modes that can be used for analysis; and (2) modal tracking under continued vibrational excitation as in a real-time, in-flight like environment. The vibrational signature of the structural device is measured directly using a suite of tri-axial accelerometers characterizing a multiple input/multiple output (*MIMO*) dynamic system. In this analysis, we have 15 tri-axial accelerometer measurements or 45 total output channels along with a single excitation also measured with a tri-axial accelerometer providing a 3-input system for processing.

We initially describe the experiment and then briefly develop the necessary background in stochastic subspace realization, discuss the algorithm and apply it to the isolated structural device, first, characterized by the set of noisy *MIMO* accelerometer measurements extracting the modal model from the data (subspace identification), extract the unique modal frequencies (modal coordinate transformation), track their evolution (real-time tracker) to evaluate the overall performance of the processor. Next we evaluate processor performance when the structural device is incorporated into a flight vehicle for further performance analysis. We summarize the results and predict performance.

1.0 INTRODUCTION

Existing flight data does not provide an accurate definition of the shock and vibration environments of critical components of the mechanical device assembly. A set of experimental ground tests were performed to characterize the shock and vibration response in the flight vehicle to support validation of a Finite Element Modal (*FEM*) developed by this Dynamic Characterization study. This study was designed to develop a combined flight vehicle and device finite element dynamic model. The model was validated with data from ground testing at a Test Facility (TF). The data is similar to that conducted for Extension and Safety programs with even more enhancements implemented.

Various test phases were accomplished during these experiments:

> *Phase 1*: examined shell and bending modes and stress wave propagation using just the aeroshell itself; and
>
> *Phase 2*: tests include the populated aeroshell with a specially instrumented guidance and surrogate, instrumented payload package assembled into a Ground Test Unit (*GTU*).

The Phase 2 tests were identical to those of Phase 1 except with the addition of the guidance and payload. Here we concentrate on the Phase 2 data which was used for *FEM* model validation (see [1] for details).

The system tests were performed with sophisticated dynamic simulators coupling test inputs calibrated to produce the flight measured response at critical locations. The test conducted at the vehicular level provides the information required to validate the structural dynamic finite element models; therefore, the measurement data is ideal to evaluate the performance of our on-line tracking algorithms. The evaluation and performance analysis of the *MIMO* identification and modal tracking based on experimental *GTU* test data for the flight vehicle tests incorporating a structural device payload is performed for the following test sets.

The *test sets* that we have considered for processor evaluations are:

- *GTU* Device Tests at LLNL–isolated payload tests — best modal information about payload;
- Flight Vehicle Free-Free Tests at TF–isolated flight vehicle tests— best flight vehicle information without payload

- Powered Flight Tests at TF—combined overall system test incorporating, flight vehicle, *GTU* and guidance package.

Device test data enables us to extract the dominant vibrational modes under the most ideal measurement system conditions. Knowledge of these underlying modal frequencies enables more effective signal pre-processing for modal frequency extraction. With this a-priori information available, we can test the processor design on the free-free flight vehicle tests enabling the effect on the device modal frequencies when coupled within the flight vehicle structure. Clearly processing this coupled system enables us to comprehend the vibrational effects and observe the modified modal frequencies. Finally, perhaps the most important data set is the powered-flight tests in which the complete flight system, flight vehicle aeroshell, device and guidance package are subjected to a variety G-force loads indicating the coupling effect of random excitations on the entire system. Here we observe the performance of the processor in actual (as close as possible) in-flight conditions enabling us to evaluate its overall performance.

Initially, the data were pre-processed based on the expected range of the modal frequencies for the *GTU*. The raw measurements were sampled at 25.6 kHz and then down-sampled to modal frequency ranges with the maximum frequency of less than 1 kHz. Bandpass filters were designed to minimize the uncertainties created by the noise from the instrumentation and the background environment. With this processing completed, multiple input/multiple output (*MIMO*) subspace realization algorithms [2] were applied to the tri-axial accelerometer measurements. Finally, the extracted modal frequencies were enhanced and smoothed with an optimal frequency tracker.

For tracking runs, we windowed the data sets with no overlapping windows and estimated the modal frequencies for each test case—the results are shown for each along with the estimates and summarized in the "tracking" tables to quantify processor performance. The pre-processed data were processed over the variety of buffer windows, the length of which depended on the number of modes selected for the identification which determined the individual section lengths as well as the number of sections available for processing. After each pre-processed section was extracted, the identifier was executed and the model obtained. The modal frequencies were then extracted from the model by performing an eigen-decomposition of the system matrix and transformed to modal space. Finally, the modal frequencies were extracted

and tracked using a frequency tracker. The ensemble statistics for each of the targeted modal frequency estimates were calculated also and presented in the subsequent tables.

The model-based modal tracking scheme for device diagnostics is illustrated conceptually in Fig. 1. Here in (a) the vibrational signature of the structural device is measured and provided as a noisy input to a modal identifier that is used to track modal frequency evolution in-flight. The detailed model-based approach for modal tracking and prediction is shown in Fig. 1 (b). After pre-processing the raw data available in a data window, the basic concept is to extract the vibrational system under consideration using system identification techniques [3], [4] in order to "fit" a state-space model to the data. Once identified, the "black-box" state model is transformed to modal coordinates where the modal frequencies are extracted through an eigen-decomposition technique [3]. Next an optimal *frequency tracker* using a Kalman filter is applied to the estimated modal frequencies to enhance and smooth these estimates producing a frequency track at each data window as they become available enabling the desired real-time track [3].

In this report, we briefly develop the necessary background in stochastic subspace realization, discuss the algorithm and apply it to the structural devices in each experimental test case and evaluate its overall performance. Our goal is to analyze processor performance to estimate its ability to provide a real-time technique for in-flight processing.

2.0 Model-Based Modal Tracking

Most structures or equivalently vibrational systems are multiple input/multiple output systems that are easily captured within the state-space framework. For instance, a linear, time-invariant mechanical system can be expressed as a second order vector-matrix, differential equation given by

$$M\ddot{\mathbf{d}}(\tau) + C_d\dot{\mathbf{d}}(\tau) + K\mathbf{d}(\tau) = B_p\mathbf{p}(\tau) \tag{1}$$

where $\mathbf{d}$ is the $N_d \times 1$ displacement vector, $\mathbf{p}$ is the $N_p \times 1$ excitation force, and M, C_d, K, are the $N_d \times N_d$ lumped mass, damping, and spring constant matrices characterizing the vibrational process model, respectively.

Defining the $2N_d$-state vector in terms of the displacement and its derivative as $\mathbf{x}(\tau) := \left[\ \mathbf{d}(\tau)\ \ |\ \ \dot{\mathbf{d}}(\tau)\ \right]$, then the continuous-time state-space representation of this process can be expressed as

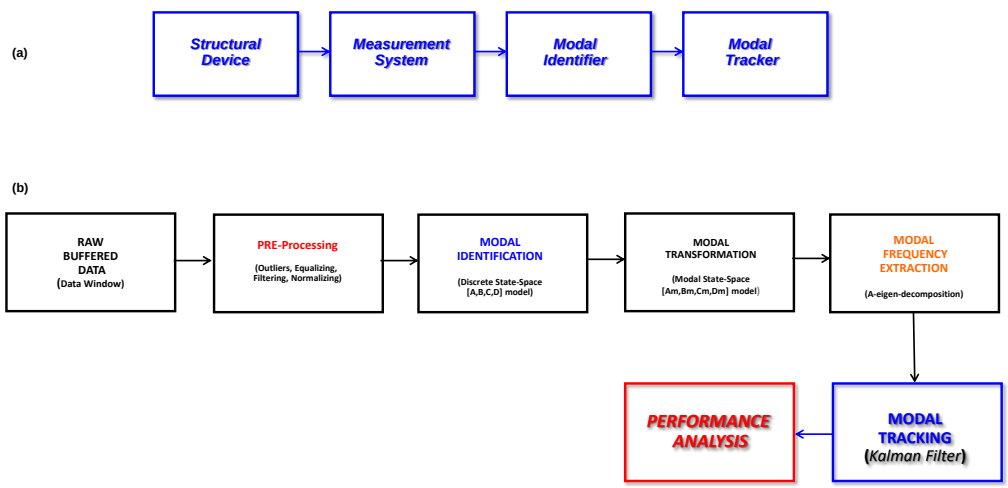

Figure 1: Processing scheme: (a) Vibration measurement/processing system, modal identifier (subspace realization), modal tracker. (b) Signal processing experimental data and performance analysis.

$$\dot{\mathbf{x}}(\tau) = \underbrace{\left[\begin{array}{c|c} 0 & I \\ --- & --- \\ -M^{-1}K & -M^{-1}C_d \end{array}\right]}_{A} \mathbf{x}(\tau) + \underbrace{\left[\begin{array}{c} 0 \\ --- \\ M^{-1}B_p \end{array}\right]}_{B} \mathbf{p}(t) \tag{2}$$

The corresponding measurement or output vector relation can be characterized by

$$\mathbf{y}(\tau) = \mathbf{C_a}\ddot{\mathbf{d}}(\tau) + \mathbf{C_v}\dot{\mathbf{d}}(\tau) + \mathbf{C_d}\mathbf{d}(\tau) \tag{3}$$

where the constant matrices: $\mathbf{C_a}, \mathbf{C_v}, \mathbf{C_d}$ are the respective acceleration, velocity and displacement weighting matrices of appropriate dimension.

In terms of the state vector relations of Eq. 2, we can express the acceleration vector as:

$$\ddot{\mathbf{d}}(\tau) = -M^{-1}K\mathbf{d}(\tau) - M^{-1}C_d\dot{\mathbf{d}}(\tau) + M^{-1}B_p\mathbf{p}(\tau) \tag{4}$$

Substituting for the acceleration term in Eq. 3, we have

$$\mathbf{y}(\tau) = \underbrace{\left[C_d - \mathbf{C_a} M^{-1} K \;\; | \;\; \mathbf{C_v} - \mathbf{C_a} M^{-1} C_d\right]}_{C} \left[\begin{array}{c} \mathbf{d}(\tau) \\ --- \\ \dot{\mathbf{d}}(\tau \end{array} \right] + \underbrace{\mathbf{C_a} M^{-1} B_p}_{D} \mathbf{p}(\tau) \tag{5}$$

to yield the vibrational measurement as:

$$\mathbf{y}(\tau) = C\mathbf{x}(\tau) + D\mathbf{u}(\tau) \tag{6}$$

where the output or measurement vector is $\mathbf{y} \in \mathcal{R}^{N_y \times 1}$ completing the multiple input/multiple output (*MIMO*) vibrational model.

2.0.1 Modal System Representation

One of the most expository representations of a mechanical system is its *modal representation* [5], [6], where the modes and mode shapes expose its internal structure and its response to various excitations. The modal representation of a system can easily be found from state-space systems by transforming the coordinates of the representation to modal space which is accomplished through an eigen-decomposition in the form of a *similarity transformation* such that the system matrices $\Sigma := \{A, B, C, D\}$ are transformed to modal coordinates by the transformation matrix T_M constructed of the eigenvectors of the underlying system [7]-[9]. That is,

$$\Big\{A, B, C, D\Big\} \longrightarrow \Big\{A_M, B_M, C_M, D_M\Big\} := \Big\{T_M A T_M^{-1} \;, T_M B, \; C T_M^{-1}, D\Big\}$$

that yields an "equivalent" system from an input/output perspective, that is, the transfer functions and impulse responses are identical.

In this coordinate system, the *modal* state solution is given by the complex modal state-space system:

$$\begin{aligned} \dot{\mathbf{x}}(\tau) &= A_M \mathbf{x}(\tau) + B_M \mathbf{u}(\tau) \\ \mathbf{y}(\tau) &= C_M \mathbf{x}(\tau) + D_M \mathbf{u}(\tau) \end{aligned} \tag{7}$$

where the system matrices become

$$A_M = \begin{bmatrix} A_{M_1} & 0 & \cdots & 0 \\ 0 & A_{M_2} & \cdots & 0 \\ \vdots & \vdots & \ddots & 0 \\ 0 & 0 & \cdots & A_{M_{N_x}} \end{bmatrix}$$

and

$$A_{M_i} = \Lambda_i = \begin{bmatrix} \sigma_i & \omega_i \\ -\omega_i & \sigma_i \end{bmatrix}$$

with

$$B_M = \begin{bmatrix} B_{M_1} \\ \vdots \\ B_{M_{N_x}} \end{bmatrix};\ C_M = \left[C_{M_1} \mid \cdots \mid C_{M_{N_x}} \right];\ D_M = D$$

Since we sample the continuous-time system, we will employ a discrete state-space representation and then transform the results back to the continuous-time domain. The generic linear, time invariant *state-space* model is defined by its system matrix A, input transmission matrix B, output or measurement matrix C and direct input feed-through matrix D for *discrete-time* systems as

$$\begin{aligned} x(t+1) &= Ax(t) + Bu(t) && \text{[State]} \\ y(t) &= Cx(t) + Du(t) && \text{[Output]} \end{aligned} \tag{8}$$

for the state $x \in R^{N_x \times 1}$, input $u \in R^{N_u \times 1}$, and output $y \in R^{N_y \times 1}$ with t an integer.

Corresponding to this representation is its sequence of impulse response matrices or Markov parameters given by

$$H(t) = CA^{t-1}B + D\delta(t) \tag{9}$$

for δ the Kronecker delta function and the equivalent discrete matrix *transfer function* in terms of the Z-transform

$$H(z) = C(zI - A)^{-1}B + D \tag{10}$$

Expanding these discrete state equations, we can show that for k-data samples ($k > N_x$), block (Hankel) matrices can be created to give both *vector* input-output (state) relations such that

$$\mathbf{y}_k(t) = \mathcal{O}_k \mathbf{x}(t) + \mathcal{T}_k \mathbf{u}(t) \tag{11}$$

with the corresponding *matrix* input-output (state) equation as

$$\mathcal{Y}_{k|2k-1} = \mathcal{O}_k \mathcal{X}_k + \mathcal{T}_k \mathcal{U}_{k|2k-1} \tag{12}$$

and the *initial states* given by

$$\mathcal{Y}_{0|k-1} = \mathcal{O}_k \mathcal{X}_0 + \mathcal{T}_k \mathcal{U}_{0|k-1} \tag{13}$$

where $\mathcal{U}_{0|k-1},\ \mathcal{Y}_{0|k-1}$ are the *past* inputs and outputs, while $\mathcal{U}_{k|2k-1},\ \mathcal{Y}_{k|2k-1}$ are the future inputs and outputs which are all *block Hankel* matrices [16]-[20].

2.0.2 Subspace Identification

Next we define the *augmented* (input-output) *data matrix* $\mathcal{D} \in \mathcal{R}^{k(N_u+N_y)\times k(N_u+N_y)}$ as

$$\mathcal{D}_{0|k-1} \quad := \quad \begin{bmatrix} \mathcal{U}_{0|k-1} \\ --- \\ \mathcal{Y}_{0|k-1} \end{bmatrix} = \begin{bmatrix} \mathbf{I} & | & 0 \\ - & & - \\ \mathcal{T}_k & | & \mathcal{O}_k \end{bmatrix} \begin{bmatrix} \mathcal{U}_{0|k-1} \\ -- \\ \mathcal{X}_0 \end{bmatrix} \tag{14}$$

Performing an orthogonal LQ-decomposition (*dual* QR-decomposition: $L = R'$, $Q = Q'$) on the data matrix, we obtain

$$\mathcal{D} = L \times Q \text{ with } L \text{ lower block triangular and } Q \text{ orthogonal} \tag{15}$$

That is,

$$L = \begin{bmatrix} L_{11} & | & 0 \\ - & - & - \\ L_{21} & | & L_{22} \end{bmatrix} \quad \text{and} \quad Q = \begin{bmatrix} Q_1' \\ -- \\ Q_2' \end{bmatrix} \text{ for } \quad Q'Q = I$$

with the $L_{11} \in \mathcal{R}^{kN_u\times 1}$, $L_{21} \in \mathcal{R}^{k(N_u+N_y)\times 1}$, and $L_{22} \in \mathcal{R}^{k(N_u+N_y)\times k(N_u+N_y)}$ and $Q \in \mathcal{R}^{N_u\times N_y}$.

Therefore, we have the LQ-decomposed data matrix as:

$$\mathcal{D}_{0|k-1} = \begin{bmatrix} \mathbf{I} & | & 0 \\ - & & - \\ \mathcal{T}_k & | & \mathcal{O}_k \end{bmatrix} \begin{bmatrix} \mathcal{U}_{0|k-1} \\ -- \\ \mathcal{X}_0 \end{bmatrix} = \begin{bmatrix} \mathbf{L}_{11} & | & 0 \\ - & & - \\ \mathbf{L}_{21} & | & \mathbf{L}_{22} \end{bmatrix} \begin{bmatrix} Q_1' \\ -- \\ Q_2' \end{bmatrix} \tag{16}$$

These expressions enable the orthogonal decomposition of $\mathcal{Y}_{0|k-1}$; therefore, it follows from Eq. 16 that

$$\mathcal{Y}_{0|k-1} = \mathcal{O}_k\mathcal{X}_0 + \mathcal{T}_k\mathcal{U}_{0|k-1} = \mathcal{O}_k\mathcal{X}_0 + \mathcal{T}_k(L_{11}Q_1') = L_{21}Q_1' + L_{22}Q_2' \tag{17}$$

and post-multiplying this expression by Q_2 with the ortho-normality/orthogonality conditions of the LQ-decomposition imposed as: $Q_2' \times Q_2 = I$ and $Q_1' \times Q_2 = 0$ gives

$$\mathcal{Y}_{0|k-1}Q_2 = \mathcal{O}_k\mathcal{X}_0Q_2 + \mathcal{T}_kL_{11}\underbrace{Q_1'Q_2}_{0} = L_{21}\underbrace{Q_1'Q_2}_{0} + L_{22}\underbrace{Q_2'Q_2}_{I} = \ L_{22}$$

or simply

$$\mathcal{O}_k \times \mathcal{X}_0 \times Q_2 \ = \ L_{22} \tag{18}$$

implying that the rank $\rho(L_{22}) = N_x$.

Therefore, performing the *SVD* of L_{22}, that is,

$$L_{22} = \left[\mathcal{U}_1 \mid \mathcal{U}_2\right] \begin{bmatrix} \Sigma_1 & | & 0 \\ - & - & - \\ 0 & | & 0 \end{bmatrix} \begin{bmatrix} \mathcal{V}_1' \\ -- \\ \mathcal{V}_2' \end{bmatrix} \tag{19}$$

yields

$$\mathcal{O}_k\mathcal{X}_0Q_2 = \mathcal{U}_1 \times \Sigma_1 \times \mathcal{V}_1' = \underbrace{(\mathcal{U}_1\Sigma_1^{1/2})}_{\mathcal{O}_k} \times \underbrace{(\Sigma_1^{T/2}\mathcal{V}_1')}_{\mathcal{C}_k} \tag{20}$$

and therefore, the system matrices are A, B, C, D can be extracted by:

$$A = \mathcal{O}^{\#}_{N_x-1} \times \mathcal{O}^{\uparrow}_{N_x}; \qquad C = \mathcal{O}(1:N_y, 1:N_x) \tag{21}$$

for $\mathcal{O}^{\#}_{N_x-1}$ the pseudo-inverse and $\mathcal{O}^{\uparrow}_{N_x}$ the shifted observability matrix (see [2] for details).

The input transmission an direct feedthrough matrices B and D can be obtained by solving a set of overdetermined linear equations (least-squares) from the following relations

$$\mathcal{L} \times \begin{bmatrix} \hat{D} \\ -- \\ \hat{B} \end{bmatrix} = \mathcal{U}_2' L_{21} L_{11}^{-1} \tag{22}$$

where $\mathcal{L}$ is a block coefficient matrix (see [16]-[21] for the details).

Therefore, we have the **M***ultivariable* **O***utput* **E***rror* **S***tate-S***P***ace* (*MOESP*) algorithm given by:

- Compute the LQ-decomposition of $\mathcal{D}$ of Eq. 16;
- Perform the *SVD* of L_{22} in Eq. 19 to extract $\mathcal{O}_k$;
- Obtain A and C from Eq. 21; and
- Solve the least-squares problem to obtain B and D from Eq. 22.

2.0.3 Modal Frequency Tracker

The overall approach to modal-frequency tracking is based on the development of robust subspace identification techniques that can be applied to solve this problem—in real-time. The main idea is to pre-process a section or window of digitized data and perform a system (vibrational) identification followed by an extraction of the underlying modes from the identified model producing raw estimates of the corresponding modal frequencies and mode shapes. Once the "raw" modal frequencies in each window are extracted an optimal sequential tracking algorithm (Kalman filter) is applied to "smooth" the estimates.

The modal frequency tracker design is a model-based processor (Kalman filter) that has been applied successfully in wide variety of applications [3], [26], [27]. The underlying frequency estimator/tracker is based on the assumption that the frequency change is constant over the sampling interval ($\dot{f}(t_{k+1}) \approx \dot{f}(t_k)$) and the model uncertainty can be characterized by Gaussian process noise leads to the following set of discrete-time, Gauss-Markov stochastic equations

$$\begin{aligned} f(t_{k+1}) &= f(t_k) + \triangle t_k \dot{f}(t_k) + w_1(t_k) && \text{[Frequency]} \\ \dot{f}(t_{k+1}) &= \dot{f}(t_k) + w_2(t_k) && \text{[Rate]} \end{aligned} \tag{23}$$

where w is zero-mean, Gaussian with $\mathbf{w} \sim \mathcal{N}(0, R_{ww})$. The corresponding measurement is also contaminated with instrumentation noise represented by zero-mean, Gaussian uncertainties as

$$y(t_k) = f(t_k) + v(t_k) \qquad \text{[Measurement]}$$

such that $v \sim \mathcal{N}(0, R_{vv})$.

A combination of both process and measurement systems can be placed in a discrete-time ($t_k \to t$), state-space framework by defining the state vector as $\mathbf{f}(t) := [f(t) \mid \dot{f}(t)]'$ giving the corresponding *Modal-Frequency Gauss-Markov model* of Eq. 23.

Now with this underlying frequency model established, we know that the optimal solution to the state estimation or frequency tracking problem is provided by the Kalman filter [3], that is,

$$\hat{\mathbf{f}}(t+1|t+1) = \hat{\mathbf{f}}(t+1|t) + K(t+1)e(t+1)$$

or component-wise (states), we have

$$\begin{aligned} \hat{f}(t+1|t+1) &= \hat{f}(t+1|t) + K_1(t+1)e(t+1) \\ \hat{\dot{f}}(t+1|t+1) &= \hat{\dot{f}}(t+1|t) + K_2(t+1)e(t+1) \\ \hat{y}(t+1|t) &= \hat{f}(t+1|t) \\ e(t+1) &= y(t+1) - \hat{y}(t+1|t) \end{aligned} \tag{24}$$

where $e(t)$ is the innovations/residual sequence and $K(t)$ are the gains or weights. This notation is defined by the conditional mean, $\hat{f}(t+1|t) := E\{f(t+1)|y(t), \cdots, y(0)\}$, that is, the estimate of $f(t+1)$ based on all of the available data up to time t.

Since we are primarily interested in a real-time application, we restrict the processor to reach steady-state in Eq. 24, that is, the Kalman gain ($K(t) \to K_{ss}$) becomes a constant (steady-state) that can *pre-calculated* directly from the discrete Riccati equation to give the frequency tracker relations [3], [26], [27].

3.0 GTU Device Test Results

The *GTU* test was performed at the Lawrence Livermore National Laboratory (*LLNL*) in conjunction with the other test sets required for the *FEM* model validation. The *LLNL* tests consisted primarily of subjecting the *GTU* to random excitations by placing a stinger or motor-driven rod perpendicular to the base of the structure. A suite of 15-tri-axial accelerometers were positioned strategically about the device surface as well as a single tri-axial sensor allocated to measure the excitation time series. In total, an array of 45-accelerometer channels acquired a set of data at a 25.6 kHz sampling frequency. The data were subsequently down-sampled to 0.4 kHz in order to focus on the targeted modal frequencies ($< 400Hz$). From the state-space perspective, we have a targeted system of up to a maximum of 14-modes or 28-states with an array of 45 channels of time series measurements and 1-channel of an excitation measurement as illustrated in Fig. 2. In this section we will discuss the processing and analysis of two data sets: *GTU* Data Set No. 5 and *GTU* Data Set No. 1.

3.0.1 GTU: Data Set No. 5

Data set No. 5 consisted of 13-tri-axial sensors placed at various locations on the surface of the device resulting in 39 (3×13 channels) time series channels along with a random excitation measured by 1 tri-axial (3-input channels) establishing a multiple input/multiple output (*MIMO*) system.

For Data set No. 5 the 13-tri-axial measurement channels along with a random force input channel were combined to produce a data set of noisy powered-flight measurements resulting in 3-input channels/39 output channels that were pre-processed by:

1. Down-sampling the measured data from 25.6 kHz to 0.4 kHz because the highest modal frequencies of interest were less than 400 Hz.

2. Bandpass filtering the down-sampled data to a frequency band of $150-385$ Hz using a 1024-weight finite impulse response (FIR) filter designed with the optimal Remez exchange algorithm available in MATLAB.

3. *MIMO* identification performing the multivariable output error state-space algorithm (*MOESP*) subspace identification approach.

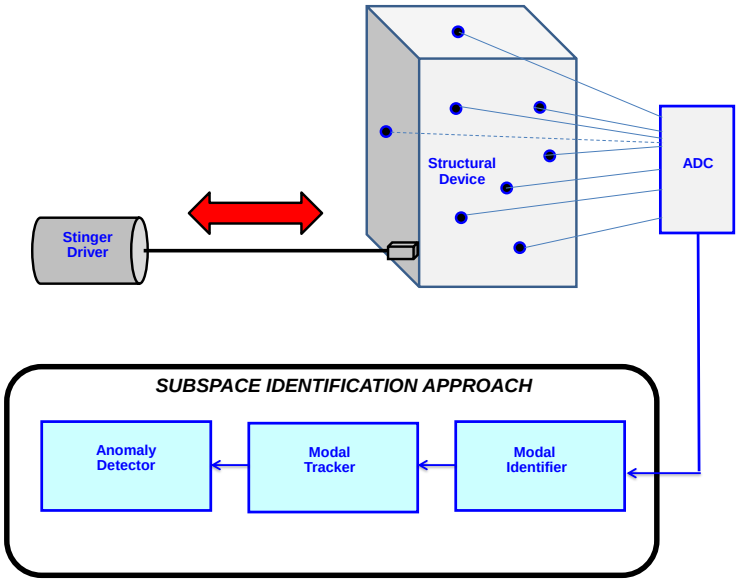

Figure 2: Structural Device Experimental Setup: Motor driven stinger random vibrations, *MIMO* ADC measurements, subspace identification: identifier, tracker, detector system.

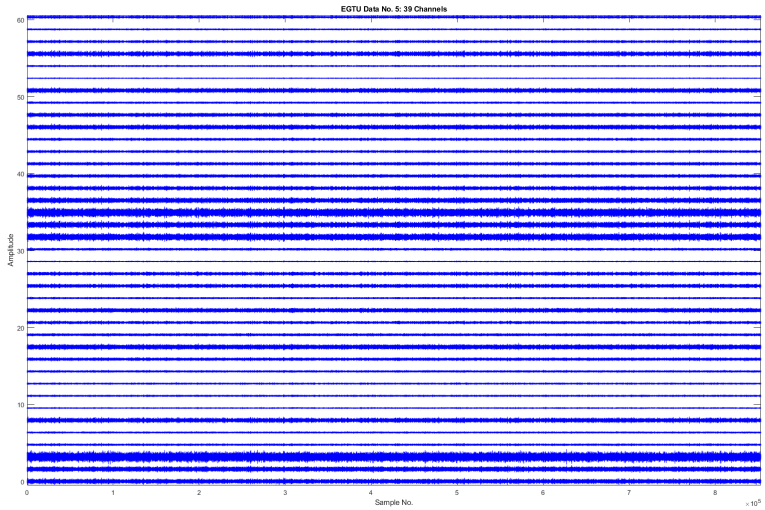

Figure 3: Raw *GTU* No. 5 Data: 39-channels or 13-tri-axial accelerometers.

The raw *MIMO* measurement is shown in Fig. 3 where we see the 39-time series channels indicating a successful measurement array. The power spectral density function of this data ensemble (green) was estimated using the average periodogram (Welch) method [3] resulting in the noisy spectra shown in Fig. 4 over the entire frequency range of the data, but only illustrating up to 6.25 kHz. The thick (red) plot is the average spectrum. Our frequency range of high interest is between $150 - 385Hz$ indicated in the figure.

After pre-processing the *GTU* device data and performing the identification for various modal model sets ranging from $7 - 15$ modes ($14 - 30$ states) the results for the Data Set No. 5 10-mode (20-state) model is shown in Fig. 5 comparing the average "identified" model spectrum (red) to the average down-sampled (blue) and the average filtered (green) spectra. The identified spectra were developed from the *MIMO* state-space model with the modal frequencies extracted (eigenvalues of the system matrix). These model frequency estimates are shown in the figure as the red-filled squares. Note how they align with the spectral peaks. Since we have identified a *MIMO* model from the data, all of the internal coupling has been incorporated through the identification process (weak as well as strong modal frequencies). Since it is a multi-channel problem, the model provides 39-impulse responses (or

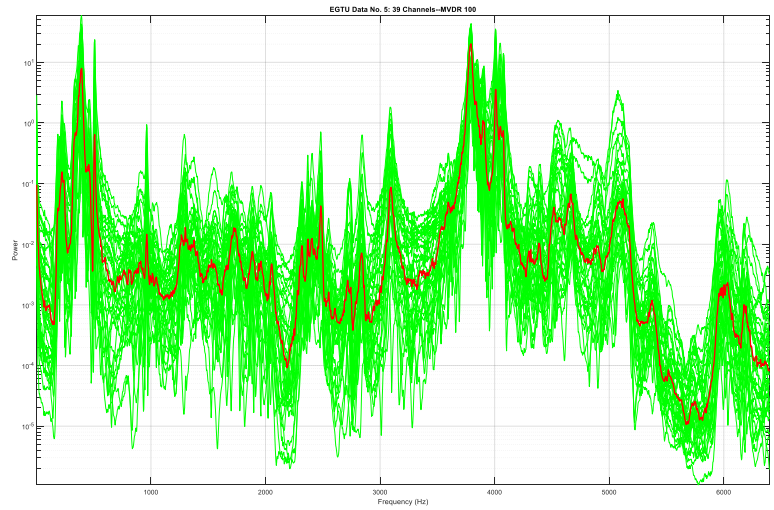

Figure 4: Raw *GTU* No. 5 Power Spectra 39-channels or 13-tri-axial accelerometers. Ensemble spectra (green), average spectrum (red).

frequency responses) — one for each measurement channel. An ensemble of these 39-frequency response power spectral estimates obtained directly from the identified model (9-mode) are shown in Fig. 6. The ensemble of spectral estimates is shown in green, while its average spectrum is red. Note how smooth the spectra have become primarily because the model is noise free and also how repeatable the spectra appear attesting to the advantage of using this model-based approach.

The results of the identification for various model orders are shown in Table 1. The trade-off is that increasing the order enables more extraneous modes to be identified along with the true-targeted (expected) modal frequencies being sought. Here we used the long data sets (time series) available ($> 25K$ samples) to perform the modal frequency identification/extraction enabling more accurate precision then that would be available from the real-time, short, buffered data windows.

We calculated the *percentage relative error* using

$$\mathcal{R}_\epsilon := \frac{\text{True Modal Frequency} \; - \; \text{Estimated Modal Frequency}}{\text{True Modal Frequency}} \times 100 \quad (25)$$

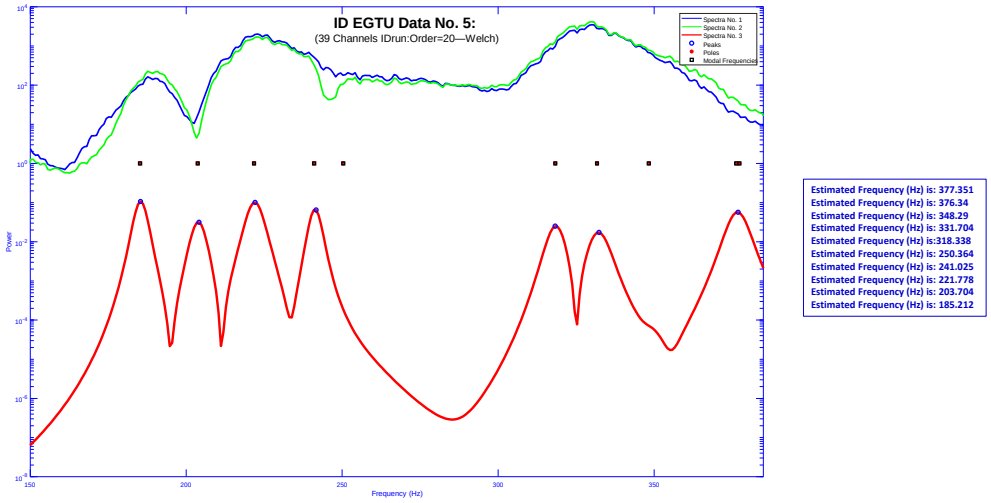

Figure 5: Estimated Average *GTU* No. 5 Spectra: Raw down-sampled spectrum (blue), filtered/down-sampled spectrum (green) and identified 10-mode spectrum (red) with modal frequency estimates (squares) from identified model.

From the table we see the relative error for each modal frequency (red parentheses) with the average relative error for each model order indicated in the last row of the table. The 15-mode model identification (30-states) yields reasonable estimates of the target modal frequencies at the cost of a larger number of extraneous frequency estimates, but provides the smallest average relative error of 0.85% identifying all of the target frequencies. The lower order estimates are reasonable, but fail to capture the modal frequency at 276 Hz. It is also interesting to note that all of the averages as well as individual errors are less than 5% (except for one individual) again attesting to a reliable model-based modal identification process.

Next, we processed the data in order to evaluate the performance of the subspace identifier on a set of buffered data window data, similar to what would be expected in-flight and in real-time. We pre-processed the data first as mentioned above by decimating and bandpass filtering, then we selected the 10-mode model (20-states) for subspace identification and provided the buffer windows to the be processed.

After the state-space model was identified and transformed to "modal space", the eigen-frequencies were estimated and each modal frequency was extracted to produce the "tracks". For the *GTU* Data Set No. 5, the tracking results are shown in Fig. 7 where we see each of the estimated modal frequencies and their corresponding $\pm 1\sigma$-confidence limits in (a) along with their corresponding histogram in (b). We note how tight the frequency estimates are bound by the confidence limits indicating a consistent estimate with few outliers in (a). The modal frequency histogram is also a good indicator of consistency, since there is little spreading of the peaks indicating a high peak (modal frequency) probability. Finally, the output of the frequency tracker of Eq. 24 shows remarkably consistent tracks after the initialization period has elapsed. To quantify the performance of the tracker we present the results in Table 2 below. In the this table we see that the frequency estimates are precise with an average standard deviation of $\pm 0.22Hz$ and a relative error of 1.7% indicating an operational tracker with outstanding performance capability.

3.0.2 GTU: Data Set No. 1

We pre-processed *GTU* Data Set No. 1 as before for Data Set No. 5 again concentrating on the targeted modal frequencies. The idea was to investigate the processor performance on a different data set employing different

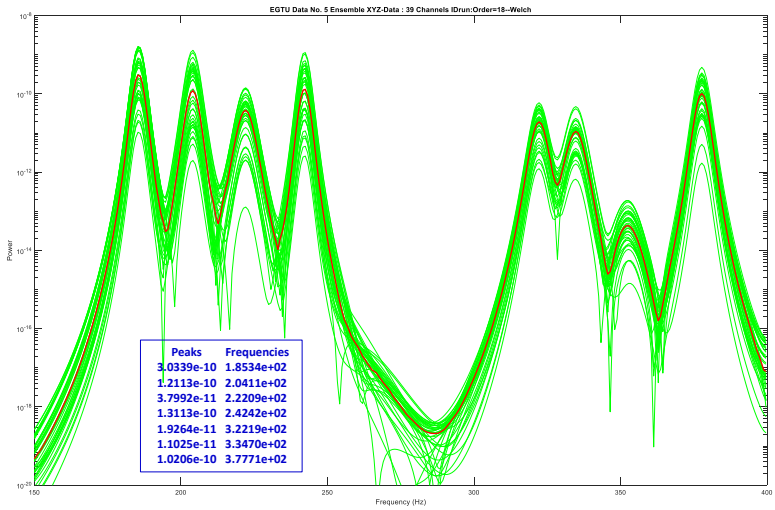

Figure 6: Identified (9-mode Model) *GTU* No. 5 Power Spectra: Ensemble (39-channels or 13-tri-axial accelerometers).

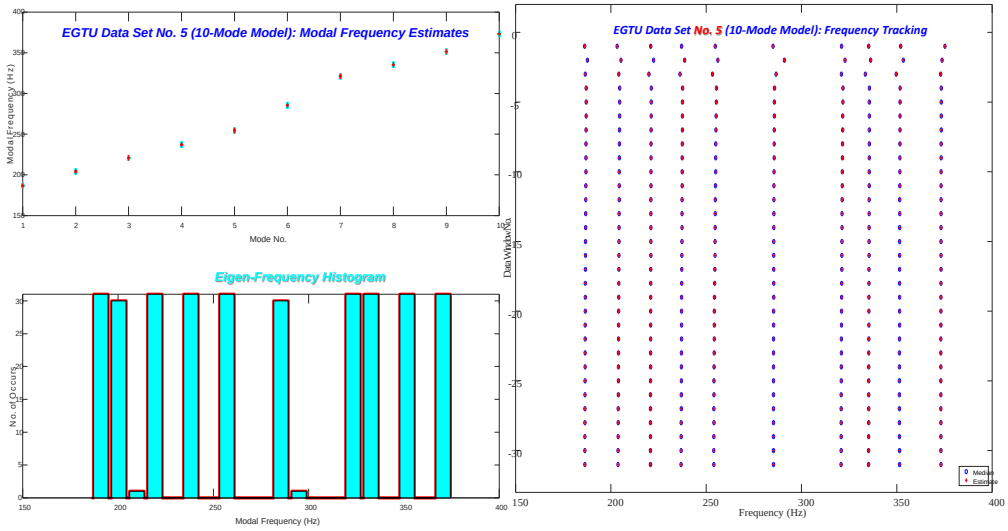

Figure 7: *GTU* No. 5 Modal Frequency Tracking Results: (a) Modal frequency estimates. (b) Frequency Histogram. (c) 10-mode model frequency tracks.

accelerometer locations than those for Data set No. 5 still employing random excitations. Data set No. 1 consisted of 9-tri-axial sensors placed at various locations on the surface of the device resulting in 27 (3×9 channels) time series channels along with the single radial axis (stinger) random force input establishing a multiple input/multiple output measurement system as before. We limited the model order to $7 - 10$ modes, since we are considering a real-time application. The results are shown for the 10-mode model (20-states) average spectra in Fig. 8 and we observe similar performance of the identifier. Table 3 indicates the performance of the processor. Both the 8-mode and 10-mode identifications provide the smallest average percentage relative errors of 1.85%, but neither was able to identify a targeted mode at 276 Hz. For the real-time scenario, the 8-mode model identifier would be the choice because of its simplicity and relative processing time — the larger the number of modes, the longer the identification period. Tracking performance of the processor on this data set was also outstanding as indicated by the precise modal frequency estimates (tight confidence limits) in Fig. 9 along with "smooth" frequency tracks. The quantified results are shown in Table 4 where we see an average deviation of $\pm 0.22 Hz$ and a slightly larger relative error of 1.9% again indicating outstanding tracker performance.

Next, we investigate the flight vehicle free-free flight measurements.

Table 1. GTU Data: **Test Set No.** 5–Modal Frequency Estimates

MODAL Frequency Estimates (Relative Error($\%\mathcal{R}_\epsilon$))					
Frequency	**7 mode**($\%\epsilon$)	**8 mode**($\%\epsilon$)	**9 mode**($\%\epsilon$)	**10 mode**($\%\epsilon$)	**15 mode**($\%\epsilon$)
179 Hz	188.1 (5.1)	186.0 (3.9)	185.4 (3.6)	185.2 (3.4)	179.0 (0.0)
204 Hz	208.3 (2.1)	205.7 (0.9)	203.8 (0.1)	203.7 (0.6)	206.5 (1.4)
218 Hz	226.3 (3.8)	224.8 (3.1)	221.8 (1.8)	221.8 (1.7)	219.2 (0.7)
247 Hz	247.5 (0.2)	245.2 (0.7)	241.9 (2.1)	250.4 (1.4)	250.2 (1.3)
276 Hz	-	-	-	-	277.7(0.6)
367 Hz	370.4 (1.0)	374.4 (2.0)	377.3 (2.8)	376.3 (2.5)	363.1 (1.1)
Avg $\%\mathcal{R}_\epsilon$	**2.44%**	**1.60%**	**2.08%**	**1.42%**	**0.85%**

Table 2. GTU Data: **Test Set No.** 5–Modal Frequency Tracking Results for 10-mode model.

MODAL Frequency Tracking (Confidence/Relative Error($\pm\sigma/\%\mathcal{R}_\epsilon$))	
Frequency	**10 modes** $\pm\,\sigma(\%\mathcal{R}_\epsilon)$
179 Hz	186.7± 0.24 (4.3)
204 Hz	204.2± 0.27 (0.1)
218 Hz	220.9± 0.13 (1.3)
247 Hz	254.5± 0.45 (3.0)
276 Hz	285.5± 0.17 (3.4)
367 Hz	373.2± 0.08 (1.7)
Avg $\pm\sigma(\%\mathcal{R}_\epsilon)$	$\pm$**0.22** (**1.7%**)

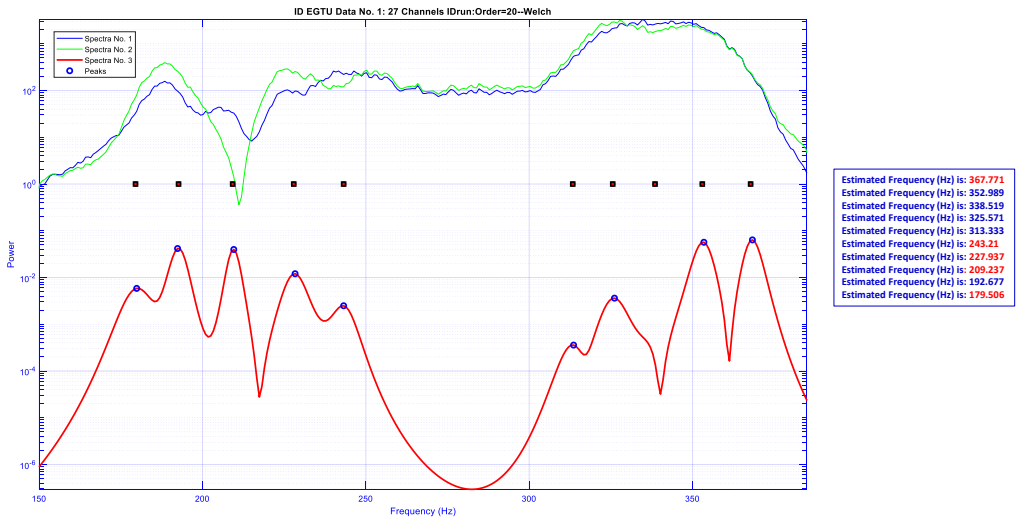

Figure 8: Estimated Average *GTU* No. 1 Spectra: Raw down-sampled spectrum (blue), filtered/down-sampled spectrum (green) and identified 10-mode spectrum (red) with modal frequency estimates (squares) from identified model.

Table 3. GTU Data: **Test Set No.** 1–Modal Frequency Estimates

MODAL Frequency Estimates (Relative Error($\%\mathcal{R}_\epsilon$))				
Frequency	**7 mode**($\%\epsilon$)	**8 mode**($\%\epsilon$)	**9 mode**($\%\epsilon$)	**10 mode**($\%\epsilon$)
179 Hz	186.0 (3.9)	184.6 (3.1)	185.0 (3.4)	179.5 (0.3)
204 Hz	205.9 (0.9)	202.0 (1.0)	200.4 (1.7)	209.2 (2.6)
218 Hz	230.8 (5.9)	225.8 (3.6)	222.5 (2.0)	227.9 (4.6)
247 Hz	247.9 (0.4)	244.1 (1.2)	242.8 (1.7)	243.2 (1.5)
276 Hz	-	-	-	-
367 Hz	359.7 (2.0)	362.4 (1.25)	363.3 (1.0)	367.8 (0.3)
Avg $\%\mathcal{R}_\epsilon$	**2.62%**	**1.86%**	**2.26%**	**1.86%**

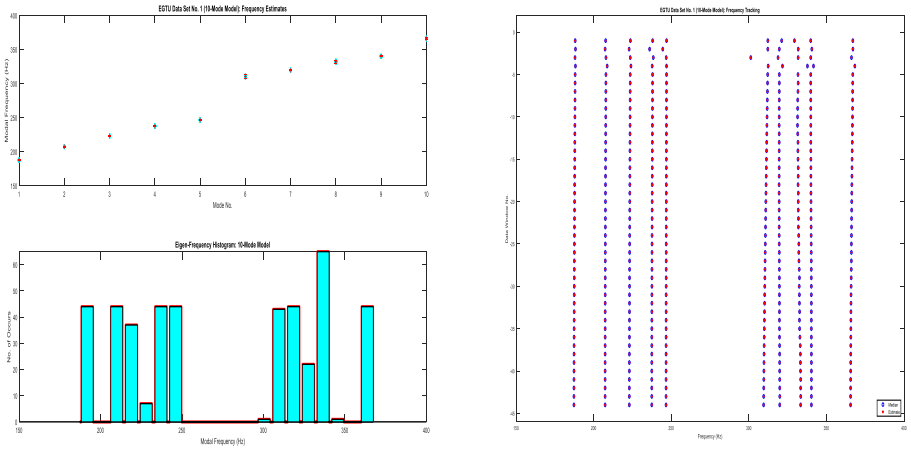

Figure 9: *GTU* No. 1 Modal Frequency Tracking Results: (a) Modal frequency estimates. (b) Frequency Histogram. (c) 10-mode model frequency tracks.

Table 4. GTU Data: **Test Set No. 1**–Modal Frequency Tracking Results for 10-mode model.

MODAL Frequency Tracking (Confidence/Relative Error($\pm\sigma/\%\mathcal{R}_\epsilon$))	
Frequency	**10 modes** $\pm\,\sigma(\%\mathcal{R}_\epsilon)$
179 Hz	187.6± 0.24 (4.8)
204 Hz	207.6± 0.17 (1.8)
218 Hz	223.2± 0.18 (2.4)
247 Hz	246.8± 0.45 (0.08)
276 Hz	-±- (-)
367 Hz	366.2± 0.08 (0.22)
Avg $\pm\sigma(\%\mathcal{R}_\epsilon)$	**±0.22 (1.9%)**

4.0 Flight Vehicle Free-Free Data: Test Results

The 15-tri-axial measurement channels along with the random stinger (force) input channel were combined to produce a data set of noisy flight vehicle free-free measurements resulting in 3 input channels/45 output channels that were pre-processed by:

1. Down-sampling the measured data from 25.6 kHz to 0.45 kHz because the highest modal frequencies of interest were less than 425 Hz.

2. Bandpass filtering the down-sampled data to a frequency band of $150-425$ Hz using a 1024-weight finite impulse response (FIR) filter designed with the optimal Remez exchange algorithm in MATLAB.

3. *MIMO* identification was performed using the multi-variable output error state-space.

After pre-processing, the *MIMO* identifier estimated the modal frequencies and the average results are shown in Fig. 10 as before for the other tests. The results of these runs for various model orders ($2\times$ no. modes) along with their relative errors are shown in Table 5. Here we see the true (best estimated) modal frequencies (green) along with the estimates for each based on the number of identified mode specified in the *MOESP* algorithm. The percentage relative errors for each estimated modal frequency is shown in red along with the corresponding average percentage (relative) error for the number of modes selected. Identifications of modal models ranging from $6-10$ modes. None of the modal identifiers were able to estimate the modal frequencies at 187 Hz (except for the 8-mode case) and 193 Hz while 5 of the 7 targeted frequencies were identified in most cases. The best performance was achieved using the 10-mode model with a percentage relative error of 2.38%. All of the identifiers were not able to obtain good estimates of the 215 Hz modal frequency with most errors exceeding 10% overestimating the value. An examination of the power spectra in Fig. 10 and Fig. 11 reveal a notch at that frequency in the measured data (blue). The ensemble spectra (green) in Fig. 11 reveals a reasonably consistent model estimator.

The frequency tracker performed well on the flight vehicle free-free data set as indicated in Fig. 12 with tight standard deviations in (a) a good

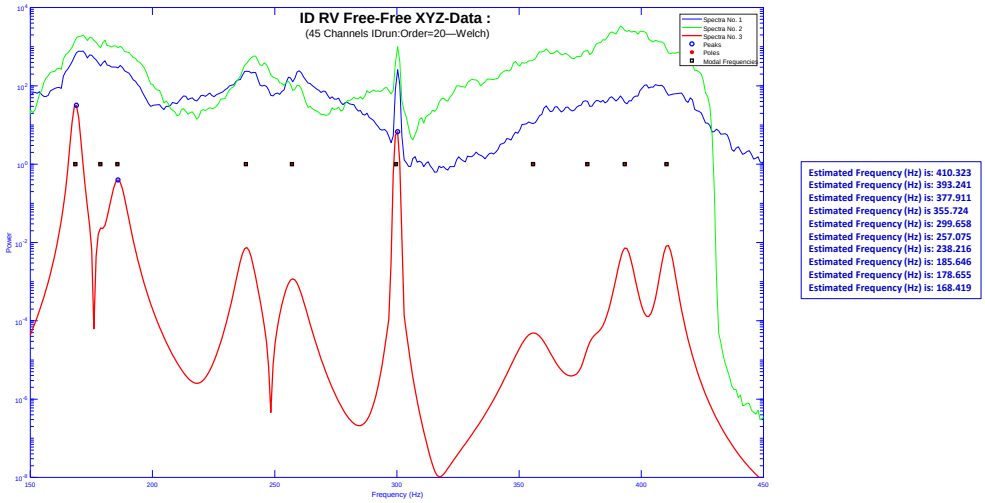

Figure 10: Estimated Average FREE-FREE Spectra: Raw down-sampled spectrum (blue), filtered/down-sampled spectrum (green) and identified 10-mode spectrum (red) with modal frequency estimates (squares) from identified model

histogram indicating distinct modal frequency estimates in (b) and smooth tracks in (c). Quantitatively from Table 6, the tracking precision of ± 0.17 indicates an outstanding tracker with a 3.8% relative error—not quite as good as the GTU results but still reasonable for this data set. Next we investigate the powered-flight data and the performance of the subspace identifier.

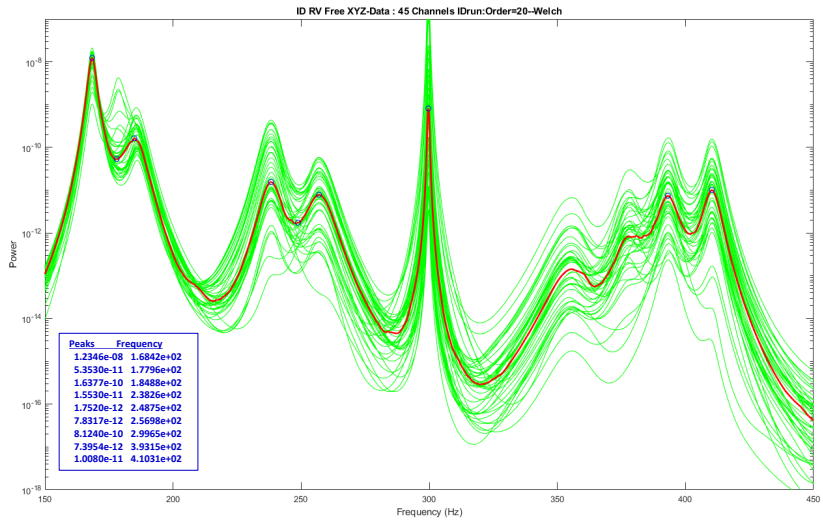

Figure 11: Estimated Ensemble Average FREE-FREE Spectra: Ensemble (45-Channel) identified 10-mode spectra (green) and average spectrum (red) with peak frequency estimates (insert).

Table 5. Flight Vehicle Data: **Flight flight vehicle Free-Free**–Modal Frequency Est.

MODAL Frequency Estimates (Relative Error($\%\mathcal{R}_\epsilon$))					
Frequency	**6 mode**($\%\epsilon$)	**7 mode**($\%\epsilon$)	**8 mode**($\%\epsilon$)	**9 mode**($\%\epsilon$)	**10 mode**($\%\epsilon$)
179 Hz	172.6 (3.6)	171.7 (4.1)	170.0 (5.0)	178.7 (0.2)	178.7 (0.2)
186 Hz	-	185.8 (0.1)	184.2 (1.0)	187.0 (0.4)	185.7 (0.2)
187 Hz	-	-	190.3 (1.8)	-	-
193 Hz	-	-	-	-	-
215 Hz	232.9 (8.3)	237.6 (10.5)	239.8 (11.6)	239.8 (11.6)	238.2 (10.8)
296 Hz	252.9 (14.6)	255.2 (13.8)	259.1 (12.5)	300.4 (1.5)	299.7 (1.3)
413 Hz	403.9 (2.2)	404.2 (2.1)	404.6 (2.0)	405.0 (1.9)	410.3 (0.7)
Avg $\%\mathcal{R}_\epsilon$	**7.18%**	**6.12%**	**5.19%**	**3.12%**	**2.38%**

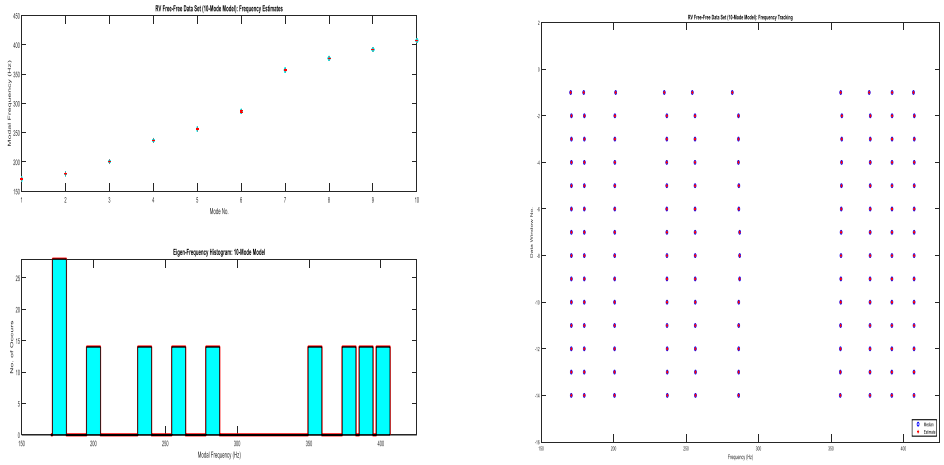

Figure 12: Flight Vehicle FREE-FREE Modal Frequency Tracking Results: (a) Modal frequency estimates. (b) Frequency Histogram. (c) 10-mode model frequency tracks.

Table 6. Flight Vehicle Free-Free Data: Modal Frequency Tracking for 10-modes

MODAL Frequency Tracking (Confidence/Relative Error($\pm\sigma/\%\mathcal{R}_\epsilon$))	
Frequency	**10 modes** $\pm\,\sigma(\%\mathcal{R}_\epsilon)$
179 Hz	179.7± 0.24 (0.4)
186 Hz	-± - (-)
187 Hz	-± - (-)
193 Hz	200.7± 0.09 (4.0)
215 Hz	236.7± 0.12 (10.1)
296 Hz	286.4± 0.32 (3.2)
413 Hz	407.3± 0.08 (1.4)
Avg $\pm\sigma(\%\mathcal{R}_\epsilon)$	±**0.17** (**3.8%**)

5.0 Powered Flight Test Results

The 15-tri-axial measurement channels along with the random force (stinger) input channel were combined to produce a data set of noisy powered-flight measurements resulting in 1-input channels/45 output channels that were pre-processed by:

1. Bandpass filtering the down-sampled data to a frequency band of $20 - 250$ Hz using a 1024-weight finite impulse response (FIR) filter designed with the optimal Remez exchange algorithm in MATLAB.

2. Due to the strong 60 Hz interference that was present during these tests a $40 - 80$ Hz, 1024-weight, FIR bandstop filter was also applied to the data making it available for the identification algorithm.

3. *MIMO* identification was performed using the multivariable output error state-space algorithm (*MOESP*) subspace identification approach.

The results of these runs for various model orders ($2\times$ no. modes) along with their relative errors are shown in Table 7. Here we see the true (best estimated) modal frequencies (green) along with the estimates for each based on the number of identified mode specified in the *MOESP* algorithm. The percentage relative errors for each estimated modal frequency is shown in red along with the corresponding average percentage (relative) error for the number of modes selected.

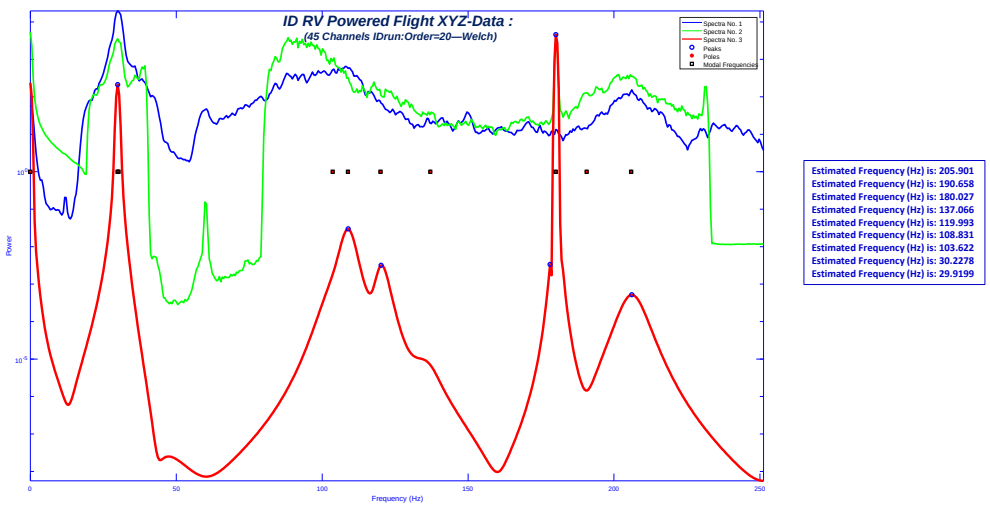

Figure 13: Estimated Average POWERED-FLIGHT Spectra: Raw down-sampled spectrum (blue), filtered/down-sampled spectrum (green) and identified 10-mode spectrum (red) with modal frequency estimates (squares) from identified model.

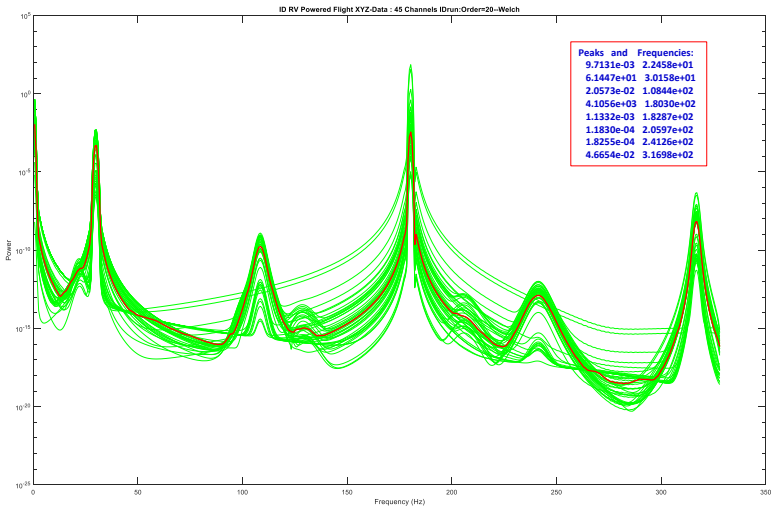

Figure 14: Estimated Ensemble Average POWERED-FLIGHT Spectra: Ensemble (45-Channel) identified 10-mode spectra (green) and average spectrum (red) with peak frequency estimates (insert).

Table 7. FLIGHT VEHICLE+GUIDANCE+PAYLOAD Data: **Powered Flight**–Frequency Est.

MODAL Frequency Estimates (Relative Error($\%\mathcal{R}_\epsilon$))					
Frequency	**6 mode**($\%\epsilon$)	**7 mode**($\%\epsilon$)	**8 mode**($\%\epsilon$)	**9 mode**($\%\epsilon$)	**10 mode**($\%\epsilon$)
31 Hz	29.9 (3.6)	31.2 (0.7)	29.9 (3.6)	29.9 (3.6)	30.2 (2.5)
103 Hz	108.1 (4.7)	108.3 (5.1)	107.5 (4.4)	108.1 (4.7)	103.6 (0.6)
114 Hz	116.2 (1.9)	118.5 (3.9)	108.5 (4.8)	108.8 (4.6)	120.0 (5.3)
142 Hz	-	167.7 (18.1)	128.2 (9.6)	128.3 (9.6)	137.1 (3.5)
181 Hz	180.0 (0.6)	180.0 (0.6)	180.0 (0.6)	180.0 (0.6)	180.0 (0.6)
221 Hz	209.1 (5.4)	251.0 (13.6)	204.9 (7.3)	205.8 (6.9)	205.9 (6.8)
Avg $\%\mathcal{R}_\epsilon$	**2.17%**	**5.05%**	**5.05%**	**5.00%**	**3.22%**

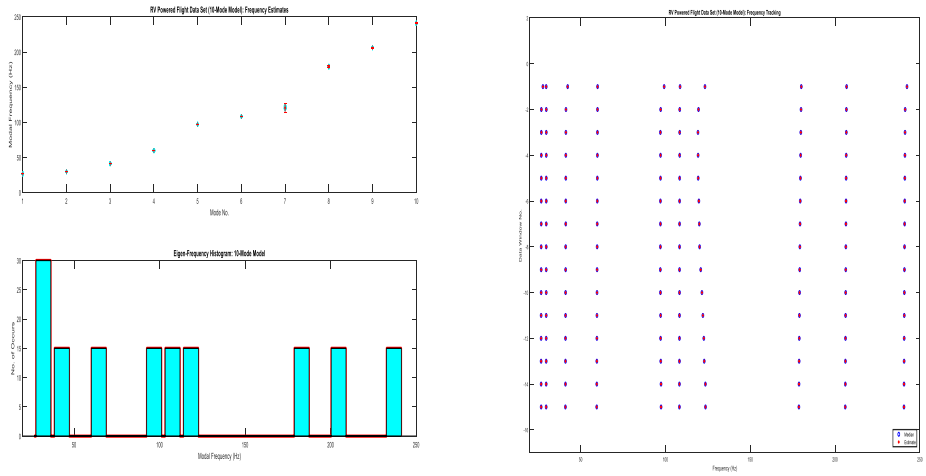

Figure 15: Flight Vehicle POWERED-FLIGHT Modal Frequency Tracking Results: (a) Modal frequency estimates. (b) Frequency Histogram. (c) 10-mode model frequency tracks.

Table 8. FLIGHT VEHICLE+GUIDANCE+PAYLOAD Data: **Powered Flight**–Modal Frequency Tracking for 10-mode model.

MODAL Frequency Tracking (Confidence/Relative Error($\pm\sigma/\%\mathcal{R}_\epsilon$))	
Frequency	**10 modes** $\pm\,\sigma(\%\mathcal{R}_\epsilon)$
31 Hz	29.7± 0.05 (3.2)
103 Hz	97.1± 0.13 (5.7)
114 Hz	108.3± 0.07 (5.0)
142 Hz	121.0± 1.67 (14.8)
181 Hz	179.2± 0.41 (1.0)
221 Hz	206.3± 0.21 (6.7)
Avg $\pm\sigma(\%\mathcal{R}_\epsilon)$	$\pm$**0.42** (**6.1%**)

For the powered flight data set, the identified model with smallest relative error is the 6-mode model, but it was not able to identify the mode at 221 Hz, while the 10-mode model with a higher relative error provided reasonable estimates of each of the predicted modal frequencies with an average relative error of 3.22%. The average identification results for the 10-mode model are shown in Fig. 13 where we see the raw down-sampled spectral data (blue), the pre-processed data (green) and the average power spectrum estimated over all 45-output channels. All of the estimated modal frequencies are shown in the inset along with their spectral locations annotated by the filled red-squares on the plot. As a glimpse of the consistency of the power spectra each of the output channel estimated impulse response power spectra from the identified model are depicted in Fig. 14 with the overlapped (green) ensemble spectra and the corresponding average spectrum shown in red. The tracking performance was *not* as good as the previous test cases but on the whole reasonable for these short data records. All of the performance metrics shown in Fig. 15 indicate a "good" tracker with tight deviations, distinct modal frequency histogram and smooth tracks; however, the quantitative results shown in Table 8 reveal some inconsistencies, especially in precise estimation of the model frequencies. These results differ from those presented in Table 7 when the long data records were used. The tracker average deviation was still reasonable at $\pm 0.42Hz$, but higher than those of the previous test cases. However, the relative error was much larger at 6.1% than even the worst case (flight vehicle free-free) at $\approx 4\%$. An examination of the individual tracks reveal that three of the targeted modal frequency tracks were at 5% relative error or higher and one track was completely missed at $\approx 15\%$ error for the targeted modal frequency at $142Hz$. Investigating the processor results for other modal orders reveals that *all* of them showed large relative errors at this modal frequency. That is none of them were capable of adequately tracking this mode.

6.0 Summary

This report summarizes the development of a model-based modal tracking scheme capable of the on-line processing of structural responses applying both system identification methods to extract a modal model and state estimation techniques to track the modal frequencies.

Background information on state-space vibrational systems was devel-

oped in Sec. 2 evolving directly to a multiple input/multiple output (*MIMO*) structural formulation. From this representation the *modal state-space* model was introduced through an eigenvalue-eigenvector formulation leading to the required similarity transformation and complex modes. Next the discrete state-space system was developed that provided the basis for the system identification methods to follow. Powerful *MIMO subspace identification* methods were discussed leading to the extraction of a modal state-space model from noisy vibrational measurements. This model provides the essential data required as input to the model-based tracking scheme.

The model-based identifier/tracker was applied to evaluate test data evolving from a vibrating system consisting of approximately 10-modes with a variety of directional tri-axial (X,Y,Z) accelerometer measurements for a total ranging from $27 - 45$-channels of noisy data. Each of the steps in developing the approach from pre-processing the raw data to subspace identification to model-based tracking were discussed in detail leading to the performance analysis of the tracking techniques completing this effort.

The results indicate that the modal frequency tracker had little difficulty in providing outstanding modal frequency tracks for the individual test cases (device, flight vehicle free-free); however, its performance for the powered flight data which included the flight vehicle, guidance and device, even though reasonable, was not as high as the previous cases. More processing of powered flight data should be performed to evaluate the processor even further.

7.0 Acknowledgments

This work performed under the auspices of the U.S. Department of Energy by Lawrence Livermore National Laboratory under Contract DE-AC52-07NA27344.

References

[1] R. Sevy and R. Eiland, "Characterization Test Plan Phases 2 & 3," *Northrup Grumman*, 9, Sept. 2013.

[2] J. V. Candy, "Anomaly detection for a vibrating structure: A subspace identification/tracking approach," *J. Acoust Soc. Am.*,vol. 142, no 2, 680=-696, 2017.

[3] J. V. Candy, *Model-Based Signal Processing*. Hoboken, N.J.:Wiley/IEEE Press, 2006.

[4] L. J. Ljung, *System Identification: Theory for the User*. Englewood Cliffs, N.J.:Prentice-Hall, 1987.

[5] M. R. Hatch, *Vibration Simulation Using MATLAB and ANSYS*. Boca Raton,FL.:Chapman and Hall/CRC Press, 2001.

[6] W. K. Gawronski, *Advanced Structural Dynamics and Active Control of Structures*. London, U.K.:Springer, 2004.

[7] T. Kailath, *Linear Systems*, Upper Saddle River, N.J.:Prentice Prentice Hall, 1980.

[8] J. G. Reid, *Linear System Fundamentals: Continuous, and Discrete, Classic and Modern*, New York, N.Y.:McGraw-Hill, 1983.

[9] R. A. DeCarlo, *Linear Systems: A State Variable Approach with Numerical Implementation*, Engelwood Cliffs, N.J.:Prentice- Hall, 1989.

[10] D. B. McCallen, "Ground Motion Estimation and Nonlinear Seismic Analysis," *Lawrence Livermore National Laboratory Report* **UCRL-JC-121667**, 1995.

[11] D. B. McCallen and A. Astaneh-Asl, "Computational Simulation of the Nonlinear Response of Suspension Bridges," *Lawrence Livermore National Laboratory Report* **UCRL-JC-128901**, 1997.

[12] J. V. Candy and R. B. Rozsa, "Safeguards design for a plutonium nitrate concentrator–an applied estimation approach." *Automatica*, **16**, 1980.

[13] J. V. Candy and E. J. Sullivan, "Ocean acoustic signal processing: a A model-based approach," *J. Acoust Soc. Am.*,vol. 92, no 6, 3185-3201, 1992.

[14] V. Wowk, *Machinery Vibration: Measurement and Analysis*. (New York:McGraw-Hill, 1991).

[15] G. H. Golub and C. F. Van Loan, *Matrix Computations*, 2nd Ed., Baltimore, MD.:The Johns Hopkins University Press, 1989.

[16] M. Aoki, *State Space Modeling of Time Series*. 2nd Ed., London, U.K.:Springer-Verlag, 1990.

[17] J. Juang, *Applied System Identification*. Upper Saddle River, N.J.:Prentice-Hall PTR, 1994.

[18] P. van Overschee and B. De Moor, *Subspace Idenification for Linear Systems: Theory, Implementation, Applications*. Boston, MA:Kluwer Academic Publishers, 1996.

[19] T. Katayama, *Subspace Methods for System Identification*. London, U.K.:Springer, 2005.

[20] M. Verhaegen and V. Verdult, *Filtering and System Identification: A least-Squares Approach*. Cambridge, U.K.:Cambridge University Press, 2007.

[21] E. Reynders, "System identification methods for (operational) modal analysis: review and comparison," *Archives of Comp. Mehtods Engr.*, Vol. 19 (1), pp. 51-124, 2012.

[22] E. Reynders, J. Houbrechts and G. De Roeck, "Fully automated (operational) modal analysis," *Mech. Sys. and Signal Proc.*, Vol. 29, pp. 228-250, 2012.

[23] V. Yaghoubi and T. Abrahamson, "The modal observability correlation as a modal correlation metric," *Topics in Modal Anal.*, vol. 7: Proc. of 31 IMAC A Confr., 2013.

[24] J. V. Candy, *Bayesian Signal Processing: Classical, Modern and Particle Filtering Methods*. 2nd Ed., Hoboken, N.J.:Wiley/IEEE Press, 2016.

[25] J. V. Candy, *Signal Processing: The Modern Approach*, New York, N.Y.:McGraw-Hill, 1988.

[26] P. R. Kalata, "The tracking index: a generalized parameter for $\alpha - \beta$ and $\alpha - \beta - \gamma$ target trackers," *IEEE Trans. Aero. and Electron. Sys.*, vol. AES-20, No. 2, pp. 174-182, 1984.

[27] J. H. Painter, D. Kerstetter and S. Jowers, "Reconciling steady-state Kalman and Alpha-Beta filter design," *IEEE Trans. Aero. and Electron. Sys.*, vol. 26, No. 6, pp. 986-991, 1990.

[28] T. Pham-Gia and T. L. Hung, "The mean and median absolute deviations," *Math. Comput. Modeling*, vol. 34, pp. 921-936, 2001.

[29] C. Leys, C. Ley, O. Klein, P. Bernard and L. Licata, "Detecting outliers: Do not use the standard deviation around the mean, use absolute deviation around the median," *J. Exper. Social Psych.*, vol. 49, pp. 764-766, 2013.

A APPENDIX:

Deterministic Subspace Identification

In this appendix, we develop the fundamental subspace realization approach to identifying the state-space representation from input-output data extending the realization from impulse response to input/output data—still assumed *deterministic*. In order to comprehend just how the deterministic realization problem can be solved when input/output sequences rather than impulse response sequences evolve, it is important to understand that most subspace realization techniques require the extraction of the extended observability matrix directly from gathered data first, followed by the system model extraction, second. The existing methods differ in the manner in which the observability matrix is estimated and its methodology for extracting the system model Σ_{ABCD}. Perhaps, the major "link" between classical realization theory employing impulse response sequences and the Hankel matrix factorization and subspace realization theory from input/output sequences lies within the inherent system theoretic "rank condition" defining the minimal dimension of the state-space, while subspace realization theory relies primarily on the concept of the persistent excitation of the input sequences as well as the minimal state-space dimension for solution [19], that is, the observability matrix spans the N_x-dimensional state-space that contains that part of the output due to the states exclusive of the inputs. In order to see this, we first construct input/output data matrices.

he discrete *LTI* solution of Eq. 8 given by

$$x(t) = A^t x(0) + \sum_{\ell=0}^{t-1} A^{t-\ell-1} B u(\ell - 1); \qquad t = 0, 1, \cdots, K \tag{26}$$

with the measurement or output system given by

$$y(t) = CA^t x(0) + \sum_{\ell=0}^{t-1} CA^{t-\ell-1} B u(\ell - 1) + D\delta(t) \tag{27}$$

Expanding this relation further over k-samples and collecting terms, we obtain

$$\begin{bmatrix} y(0) \\ y(1) \\ \vdots \\ y(k-1) \end{bmatrix} = \underbrace{\begin{bmatrix} C \\ CA \\ \vdots \\ CA^{t-k-1} \end{bmatrix}}_{\mathcal{O}_k} x(0) + \underbrace{\begin{bmatrix} D & & \cdots & 0 \\ CB & D & \cdots & 0 \\ \vdots & \vdots & \vdots & \vdots \\ CA^{k-1}B & \cdots & CB & D \end{bmatrix}}_{\mathcal{T}_k} \begin{bmatrix} u(0) \\ u(1) \\ \vdots \\ u(k-1) \end{bmatrix} \tag{28}$$

where $\mathcal{O}_k \in \mathcal{R}^{kN_y \times N_x}$ is the *observability matrix* and $\mathcal{T}_k \in \mathcal{R}^{kN_y \times kN_u}$ is *impulse response matrix*—a Toeplitz matrix [3].

Shifting these relations in time ($0 \to t$) yields

$$\begin{bmatrix} y(t) \\ y(t+1) \\ \vdots \\ y(t+k-1) \end{bmatrix} = \mathcal{O}_k x(t) + \mathcal{T}_k \begin{bmatrix} u(t) \\ u(t+1) \\ \vdots \\ u(t+k-1) \end{bmatrix} \tag{29}$$

leads to the *vector* input/output relation

$$\mathbf{y}_k(t) = \mathcal{O}_k \mathbf{x}(t) + \mathcal{T}_k \mathbf{u}_k(t) \tag{30}$$

where $\mathbf{y} \in \mathcal{R}^{kN_y \times 1}$, $\mathbf{x} \in \mathcal{R}^{N_x \times 1}$ and $\mathbf{u} \in \mathcal{R}^{kN_u \times 1}$.

We catenate these vectors to create batch data (*block Hankel*) matrices to obtain the subsequent "data equation". That is, defining the block output data matrix ($\mathcal{Y}_{0|k-1}$) and block input data matrix ($\mathcal{U}_{0|k-1}$)[1] over K-samples are:

$$\mathcal{Y}_{0|k-1} := \begin{bmatrix} \mathbf{y}(0) & \mathbf{y}(1) & \cdots & \mathbf{y}(K-1) \\ \mathbf{y}(1) & \mathbf{y}(2) & \cdots & \mathbf{y}(K) \\ \vdots & \vdots & \vdots & \vdots \\ \mathbf{y}(k-1) & \mathbf{y}(k) & \cdots & \mathbf{y}(K+k-2) \end{bmatrix} \tag{31}$$

and

$$\mathcal{U}_{0|k-1} := \begin{bmatrix} \mathbf{u}(0) & \mathbf{u}(1) & \cdots & \mathbf{u}(K-1) \\ \mathbf{u}(1) & \mathbf{u}(2) & \cdots & \mathbf{u}(K) \\ \vdots & \vdots & \vdots & \vdots \\ \mathbf{u}k-1) & \mathbf{u}(k) & \cdots & \mathbf{u}(K+k-2) \end{bmatrix} \tag{32}$$

[1]The notation "$0|k-1$" defines the first and last column element of the data matrix.

or more compactly

$$\begin{aligned}\mathcal{Y}_{0|k-1} &= \begin{bmatrix}\mathbf{y}_k(0) & \cdots & \mathbf{y}_k(K-1)\end{bmatrix} \in \mathcal{R}^{kN_y \times K} \\ \mathcal{U}_{0|k-1} &= \begin{bmatrix}\mathbf{u}_k(t) & \cdots & \mathbf{u}_k(K-1)\end{bmatrix} \in \mathcal{R}^{kN_u \times K}\end{aligned} \tag{33}$$

with the corresponding state vector defined by

$$\mathcal{X}_{0|k-1} := \begin{bmatrix}\mathbf{x}(0) & \mathbf{x}(1) & \cdots & \mathbf{x}(K-1)\end{bmatrix} \in \mathcal{R}^{N_x \times K} \tag{34}$$

Therefore, we have the *vector-matrix* input/output equation or the *data equation* that relates the system model to the data (input, state and output matrices)

$$\mathcal{Y}_{0|k-1} = \mathcal{O}_k \mathcal{X}_{0|k-1} + \mathcal{T}_k \mathcal{U}_{0|k-1} \tag{35}$$

Similarly, defining the data matrices for the samples ranging from k-to-$(2k-1)$, we have

$$\mathcal{Y}_{k|2k-1} := \begin{bmatrix} \mathbf{y}(k) & \mathbf{y}(k+1) & \cdots & \mathbf{y}(K+k-1) \\ \mathbf{y}(k+1) & \mathbf{y}(k+2) & \cdots & \mathbf{y}(K+k) \\ \vdots & \vdots & \vdots & \vdots \\ \mathbf{y}(2k-1) & \mathbf{y}(2k) & \cdots & \mathbf{y}(K+2k-2) \end{bmatrix} \tag{36}$$

and

$$\mathcal{U}_{k|2k-1} := \begin{bmatrix} \mathbf{u}(k) & \mathbf{u}(k+1) & \cdots & \mathbf{u}(K+k-1) \\ \mathbf{u}(k+1) & \mathbf{u}(k+2) & \cdots & \mathbf{u}(K+k) \\ \vdots & \vdots & \vdots & \vdots \\ \mathbf{u}(2k-1) & \mathbf{u}(2k) & \cdots & \mathbf{u}(K+2k-2) \end{bmatrix} \tag{37}$$

Again leading to the corresponding *data equation* given by

$$\mathcal{Y}_{k|2k-1} = \mathcal{O}_k \mathcal{X}_{k|2k-1} + \mathcal{T}_k \mathcal{U}_{k|2k-1} \tag{38}$$

where the block (Hankel) matrices are defined as before to give

$$\begin{aligned}\mathcal{U}_{k|2k-1} &= \begin{bmatrix}\mathbf{u}_k(k) & \mathbf{u}_k(k+1) & \cdots & \mathbf{u}_k(K+k-1)\end{bmatrix} \in \mathcal{R}^{kN_u \times K} \\ \mathcal{Y}_{k|2k-1} &= \begin{bmatrix}\mathbf{y}_k(k) & \mathbf{u}_k(k+1) & \cdots & \mathbf{y}_k(K+k-1)\end{bmatrix} \in \mathcal{R}^{kN_y \times K}\end{aligned}$$

$$\mathcal{X}_{k|2k-1} \;=\; \Big[\mathbf{x}(k) \;\; \mathbf{x}(k+1) \;\; \cdots \;\; \mathbf{x}(K+k-1) \;\Big] \in \mathcal{R}^{N_x \times K}$$

Here $\mathcal{U}_{0|k-1},\ \mathcal{Y}_{0|k-1}$ are defined as the *past* inputs and outputs (U_p,Y_p), while $\mathcal{U}_{k|2k-1},\ \mathcal{Y}_{k|2k-1}$ are the *future* inputs and outputs(U_f,Y_f) which are all *block Hankel* matrices.[14–16]

With the data equation of Eq. 38 available, we can develop the "rank condition" for input/output sequences from a least-squares viewpoint [3]. The idea is to develop a projection operator that is orthogonal to the input space $\mathcal{U}$ such that $<\mathcal{U},\mathcal{P}>=\mathbf{0}$.

To accomplish this, we minimize the cost function $\mathcal{J}$ with respect to $\mathcal{T}_k$, then the problem becomes

$$\mathcal{J} = \min_{\mathcal{T}_k} \;\; \| \, \mathcal{Y}_{k|2k-1} - \mathcal{T}_k \mathcal{U}_{k|2k-1} \, \| \tag{39}$$

which can be achieved by setting the gradient operator to zero ($\nabla_{\mathcal{T}}\mathcal{J} = \mathbf{0}$) and solving for $\hat{\mathcal{T}}_k$ leading to the well-known least-squares solution assuming $\mathcal{U}_{k|2k-1}$ is full rank ($\rho(\mathcal{U}) = kN_u$). Therefore, the orthogonal (compliment) projection operator ($\mathcal{P}^{\perp}$) operating on the data space $\mathcal{Y}$ projects the data matrix $\mathcal{Y}_{k|2k-1}$ onto the null space of $\mathcal{U}$. The orthogonal compliment operator is given by

$$\mathcal{P}_{\mathcal{U}}^{\perp} = \mathbf{I} - \mathcal{P}_{\mathcal{U}} := \mathbf{I} - \hat{\mathcal{T}}_k \times \mathcal{U}_{k|2k-1} = \mathbf{I} - \mathcal{U}'_{k|2k-1}\Big(\mathcal{U}_{k|2k-1}\mathcal{U}'_{k|2k-1}\Big)^{-1}\mathcal{U}_{k|2k-1} \tag{40}$$

where the least-squares estimate is defined as

$$\hat{\mathcal{T}}_k := \mathcal{U}'_{k|2k-1}\Big(\mathcal{U}_{k|2k-1}\mathcal{U}'_{k|2k-1}\Big)^{-1} \tag{41}$$

and therefore

$$\mathcal{Y}_{k|2k-1} \times \mathcal{P}_{\mathcal{U}}^{\perp} = \mathcal{Y}_{k|2k-1} \times \Big(\mathbf{I} - \hat{\mathcal{T}}_k \, \mathcal{U}_{k|2k-1}\Big) = \mathcal{Y}_{k|2k-1} - \hat{\mathcal{T}}_k \mathcal{U}_{k|2k-1} \tag{42}$$

Further from projection theory (orthogonal compliment), we have the orthogonality condition that

$$<\mathcal{U},\mathcal{P}> \quad \Longrightarrow \quad \mathcal{U}_{k|2k-1} \times \mathcal{P}_{\mathcal{U}}^{\perp} = \mathbf{0} \tag{43}$$

Applying the projection operator to the data equation of Eq. 38 gives

$$\mathcal{Y}_{k|2k-1} \times \mathcal{P}_{\mathcal{U}}^{\perp} = \mathcal{O}_k \mathcal{X}_{k|2k-1} \times \mathcal{P}_{\mathcal{U}}^{\perp} + \mathcal{T}_k \underbrace{\mathcal{U}_{k|2k-1}\ \mathcal{P}_{\mathcal{U}}^{\perp}}_{\mathbf{0}} = \mathcal{O}_k \mathcal{X}_{k|2k-1}\ \mathcal{P}_{\mathcal{U}}^{\perp} \tag{44}$$

and since

$$\rho\Big(\mathcal{X}_{k|2k-1}\ \mathcal{P}_{\mathcal{U}}^{\perp}\Big) = N_x$$

Taking the *SVD* of Eq. 44 decomposes the output space into the *signal subspace* and the *noise subspace* to give:

$$\mathcal{Y}_{k|2k-1}\mathcal{P}_{\mathcal{U}}^{\perp} = [U_S \mid U_N] \begin{bmatrix} \Lambda_S & | & \mathbf{0} \\ - & - & - \\ \mathbf{0} & | & \Lambda_N \end{bmatrix} \begin{bmatrix} V_S' \\ -- \\ V_N' \end{bmatrix} = \underbrace{U_S \Lambda_S V_S'}_{\text{Signal Subspace}} + \underbrace{U_N \Lambda_N V_N'}_{\text{Noise Subspace}} \tag{45}$$

From a balanced realization choice (see [2]), the observability matrix can be extracted directly through this decomposition as

$$\mathcal{O}_k \mathcal{X}_{k|2k-1}\ \mathcal{P}_{\mathcal{U}}^{\perp} = \underbrace{\Big(U_S \Lambda_S^{1/2}\Big)}_{\mathcal{O}_k} \times \Big((\Lambda_S')^{1/2} V_S'\Big) \tag{46}$$

assuming the noise subspace is negligible ($\Lambda_N(i,i) << 0\ \forall\ i$).

Even though theoretically this result is pleasing, it is not numerically efficient leading us to the linear algebraic solution to this state-space identification problem.

A.1 Multivariable Output Error State-Space (*MOESP*) Algorithm

From the data equation of Eq. 35, we can construct the *augmented* (input-output) *data matrix*, $\mathcal{D} \in \mathcal{R}^{k(N_u+N_y)\times K}$, as

$$\mathcal{D}_{0|k-1} \quad := \quad \begin{bmatrix} \mathcal{U}_{0|k-1} \\ - - - \\ \mathcal{Y}_{0|k-1} \end{bmatrix} = \begin{bmatrix} \mathbf{I}_{kN_u} & | & 0 \\ - & & - \\ \mathcal{T}_k & | & \mathcal{O}_k \end{bmatrix} \begin{bmatrix} \mathcal{U}_{0|k-1} \\ -- \\ \mathcal{X}_0 \end{bmatrix} \tag{47}$$

Performing an orthogonal LQ-decomposition (*dual* QR-decomposition: $L = R'$, $Q = Q'$) on the data matrix, we obtain

$$\mathcal{D} = L \times Q \text{ with } L \text{ lower block triangular; and } Q \text{ orthogonal} \tag{48}$$

and $L \in \mathcal{R}^{k(N_u+N_y)\times(kN_u+N_x)}$; and $Q \in \mathcal{R}^{(kN_u+N_x)\times K}$ with the decomposition in sub-matrices as

$$L = \begin{bmatrix} L_{11} & | & 0 \\ - & - & - \\ L_{21} & | & L_{22} \end{bmatrix} \quad \text{and} \quad Q = \begin{bmatrix} Q_1' \\ -- \\ Q_2' \end{bmatrix} \text{ for } \quad Q'Q = I$$

with the $L_{11} \in \mathcal{R}^{kN_u\times kN_u}$, $L_{21} \in \mathcal{R}^{kN_y\times kN_u}$, $L_{22} \in \mathcal{R}^{kN_y\times N_x}$; $Q_1' \in R^{kN_u\times K}$ and $Q_2' \in R^{N_x\times N_x}$.

Therefore, we have the LQ-decomposed data matrix as:

$$\mathcal{D}_{0|k-1} = \begin{bmatrix} \mathbf{I}_{kN_u} & | & 0 \\ - & & - \\ \mathcal{T}_k & | & \mathcal{O}_k \end{bmatrix} \begin{bmatrix} \mathcal{U}_{0|k-1} \\ -- \\ \mathcal{X}_0 \end{bmatrix} = \begin{bmatrix} \mathbf{L}_{11} & | & 0 \\ - & & - \\ \mathbf{L}_{21} & | & \mathbf{L}_{22} \end{bmatrix} \begin{bmatrix} Q_1' \\ -- \\ Q_2' \end{bmatrix} \tag{49}$$

These expressions enable the orthogonal decomposition of $\mathcal{Y}_{0|k-1}$; therefore, multiplying the sub-matrices, it follows from Eq. 49 that

$$\mathcal{Y}_{0|k-1} = \mathcal{O}_k\mathcal{X}_0 + \mathcal{T}_k\mathcal{U}_{0|k-1} = \mathcal{O}_k\mathcal{X}_0 + \mathcal{T}_k(L_{11}Q_1') = L_{21}Q_1' + L_{22}Q_2' \tag{50}$$

Post-multiplying this expression by Q_2 and imposing the ortho-normality/orthogonality conditions of the LQ-decomposition as: $Q_2' \times Q_2 = I$ and $Q_1' \times Q_2 = 0$ gives

$$\mathcal{Y}_{0|k-1}Q_2 = \mathcal{O}_k\mathcal{X}_0Q_2 + \mathcal{T}_kL_{11}\underbrace{Q_1'Q_2}_{0} = L_{21}\underbrace{Q_1'Q_2}_{0} + L_{22}\underbrace{Q_2'Q_2}_{I} = L_{22}$$

or simply

$$\mathcal{O}_k\mathcal{X}_0Q_2 = L_{22} \tag{51}$$

which implies that the rank $\rho(L_{22}) = N_x$.

Therefore, performing the *SVD* of L_{22}, that is,

$$L_{22} = \left[\mathcal{U}_1 \mid \mathcal{U}_2\right] \begin{bmatrix} \Sigma_1 & | & 0 \\ - & - & - \\ 0 & | & 0 \end{bmatrix} \begin{bmatrix} \mathcal{V}_1' \\ -- \\ \mathcal{V}_2' \end{bmatrix} \tag{52}$$

yields

$$\mathcal{O}_k \mathcal{X}_0 Q_2 = \mathcal{U}_1 \times \Sigma_1 \times \mathcal{V}_1' = \underbrace{(\mathcal{U}_1 \Sigma_1^{1/2})}_{\mathcal{O}_k} \times (\Sigma_1^{T/2} \mathcal{V}_1') \tag{53}$$

The system matrices A, B, C, D can be extracted by:

$$A = \mathcal{O}_{N_x-1}^{\#} \times \mathcal{O}_{N_x}^{\uparrow}; \qquad C = \mathcal{O}(1 : N_y, 1 : N_x) \tag{54}$$

with B and D obtained by solving a least-squares problem directly, since pre-multiplying Eq. **??** by $\mathcal{U}_2'$ gives

$$\mathcal{U}_2' \mathcal{O}_k \mathcal{X}_0 + \mathcal{U}_2' \mathcal{T}_k \mathcal{U}_{0|k-1} = \mathcal{U}_2' L_{21} Q_1' + \mathcal{U}_2' L_{22} Q_2'$$

but after substituting for $\mathcal{U}_{0|k-1}$ and applying the orthogonality conditions $\mathcal{U}_2' \mathcal{O}_k = 0$ and $\mathcal{U}_2' L_{22} = 0$, we have

$$\mathcal{U}_2' \mathcal{T}_k (L_{11} Q_1') = \mathcal{U}_2' L_{21} Q_1'$$

post-multiply by Q_1 and using its orthonormal property ($Q_1' Q_1 = I$) gives

$$\mathcal{U}_2' \mathcal{T}_k = \mathcal{U}_2' L_{21} \times L_{11}^{-1} \tag{55}$$

leading to an overdetermined set of linear equations and a least-squares solution

$$\mathcal{L} \times \begin{bmatrix} \hat{D} \\ -- \\ \hat{B} \end{bmatrix} = \mathcal{U}_2' L_{21} L_{11}^{-1} \tag{56}$$

where $\mathcal{L}$ is a block coefficient matrix (see Refr. 15 for the details).

Therefore, we have the **M***ultivariable* **O***utput* **E***rror* **S***tate-S***P***ace* (*MOESP*) algorithm given by:

- Compute the LQ-decomposition of $\mathcal{D}$ of Eq. 49;
- Perform the *SVD* of L_{22} in Eq. 52 to extract $\mathcal{O}_k$;
- Obtain A and C from Eq. 54; and
- Solve the least-squares problem to obtain B and D from Eq. 56.